

# Volumetric Representation Assisted Internal Ballistics

## Research Project

Author: Nitsan Geter  
Advisor: Dr. Yuval Levy

Department of Aerospace Engineering  
Technion - Israel Institute of Technology

October 2025

### Abstract

This work presents a coupled theoretical and numerical investigation of the internal ballistics of solid rocket motors (SRMs) with volumetric grain regression. The study focuses on AP/HTPB composite propellants and employs Saint-Robert's law to model the pressure-dependent surface regression. A Python-controlled framework integrates combustion modeling with a high-resolution finite-volume flow solver, enabling dynamic mesh deformation that tracks the evolution of the burning surface over time. Combustion characteristics, including flame temperature and characteristic velocity, are extracted from equilibrium simulations performed using NASA CEA. Empirical burn rate parameters are selected from literature and validated against the formulation's thermochemical assumptions. The framework is applied to both axisymmetric and quarter-cylinder configurations. Validation is carried out by cross-comparing the axisymmetric results with an established reference, while the three-dimensional extension is evaluated through direct comparison with the axisymmetric baseline. In addition, the 3D configuration enables the evaluation of integral performance metrics, including the instantaneous thrust and thrust coefficient, providing a more complete assessment of the motor's ballistic response. Ultimately, the simulations demonstrate that fully coupled burnback modeling is essential for capturing the coupled evolution of internal flow, pressure, and performance in SRMs.

## Nomenclature

$Q$	Vector of conserved variables	$\mathbf{F}_c$	Convective flux vector
$\mathbf{F}_d$	Diffusive flux vector	$S$	Source term vector
$\rho$	Density	$u, v, w$	Velocity components
$E$	Total energy (conserved)	$p$	Pressure
$T$	Temperature	$Y_k$	Mass fraction of species $k$
$\dot{r}$	Linear burn rate	$a$	Burn rate pre-exponential coefficient
$P_c$	Chamber pressure	$n$	Burn rate pressure exponent
$t$	Time	$\Delta t$	Time-step increment
$dr$	Local regression increment	$r(t)$	Cumulative burnback depth
$F$	Thrust	$\lambda$	Nozzle divergence correction factor
$\dot{m}$	Mass flow rate of exhaust gases	$U_e$	Nozzle exit velocity
$P_e$	Exit static pressure	$P_a$	Ambient pressure
$A_e$	Nozzle exit area	$\alpha_d$	Nozzle divergence half-angle
$\rho_p$	Propellant density	$A_b(t)$	Burning surface area
$D_{in}$	Instantaneous port diameter	$L$	Grain length
$C_F$	Thrust coefficient	$A_t$	Nozzle throat area
$O/F$	Oxidizer-to-fuel mass ratio	$T_c$	Chamber (adiabatic flame) temperature
$c^*$	Characteristic velocity	$I_{sp}$	Vacuum specific impulse
$M$	Mach number	$x$	Axial coordinate
$D_t$	Nozzle throat diameter	$D_e$	Nozzle exit diameter

# 1 Introduction

Solid rocket motors (SRMs) represent a cornerstone of modern propulsion systems due to their mechanical simplicity, reliability, and long-term storability<sup>[1]</sup>. These motors are extensively employed in space launchers, missiles, and booster stages, offering high thrust-to-weight ratios and fast response. However, accurate prediction of internal ballistics remains a non-trivial challenge, especially for motors operating under non-steady or high-pressure regimes<sup>[2]</sup>.

A fundamental aspect of SRM behavior is the regression of the solid propellant surface due to combustion. This dynamic boundary recession affects the burning surface area, the chamber pressure, and the thrust profile. Precise modeling of this regression, known as burnback, is essential for predicting the motor's performance and ensuring structural integrity during operation<sup>[3, 4]</sup>.

Traditionally, burn rate behavior is modeled using empirical pressure-dependent laws, particularly Saint-Robert's law<sup>[4, 5]</sup>, which relates local pressure to the linear regression velocity of the solid grain. However, when integrated into time-dependent simulations, this relationship becomes highly nonlinear due to mutual feedback between pressure buildup and propellant surface regression. As such, there is a need for coupled numerical frameworks that can resolve the pressure field while dynamically updating the inner boundary of the solid domain<sup>[2]</sup>.

This study introduces a numerical simulation framework designed to capture the evolution of the burning surface in solid rocket grains with dynamically changing geometries. The methodology couples an external flow solver with Python-based scripting to model burnback progression through time-dependent regression laws. Simulation parameters are drawn from literature on AP/HTPB propellants<sup>[6, 7, 8]</sup>, while thermochemical properties are obtained via NASA's CEA code<sup>[9]</sup>. The framework is first applied to a 2D axisymmetric configuration and validated against predictions from a well-established structured solver through comparison of regression depth and chamber pressure histories. Following a successful 2D validation, the approach is extended to a 3D quarter-cylinder configuration and benchmarked against the axisymmetric results. The 3D model further enables the extraction of integral performance parameters, including the instantaneous thrust and thrust coefficient, providing a direct link between internal flow evolution and the overall ballistic performance of the motor.

## 2 Theoretical Background

The internal ballistics of solid rocket motors (SRMs) involve the coupled processes of propellant surface regression and chamber pressure evolution. This section outlines the fundamental relations governing surface regression, flowfield dynamics, pressure development during the transient combustion process, as well as the resulting thrust and thrust coefficient formulations that characterize the overall motor performance.

### 2.1 Governing Equations & Pressure Evolution

The internal ballistics are governed by the compressible Navier-Stokes equations for multi-component gas flows under chemical equilibrium assumptions, formulated in the following conservation law form:

$$\frac{\partial Q}{\partial t} + \nabla \cdot (\mathbf{F}_c - \mathbf{F}_d) = S \quad (1)$$

where:

- $Q$  is the vector of conserved variables:

$$Q = \begin{bmatrix} \rho \\ \rho u \\ \rho v \\ \rho w \\ E \\ \rho_1 \\ \vdots \\ \rho_N \end{bmatrix}$$

- $\mathbf{F}_c$  and  $\mathbf{F}_d$  are the convective and diffusive flux vectors, respectively, accounting for transport of mass, momentum, energy, and chemical species.
- $S$  is the source term vector, incorporating mass generation from surface regression and chemical reactions if present.

Thermodynamic closure is obtained not through the ideal gas law, but from precomputed chemical equilibrium tables, linking pressure to density, temperature, and species mass fractions:

$$p = p(\rho, T, Y_k) \quad (2)$$

Thus, pressure evolution during the combustion process naturally emerges from the conservation equations and the equilibrium thermodynamic relationships, accurately capturing the behavior of multi-species reactive flows.

## 2.2 Pressure-Dependent Burn Rate

The linear burn rate  $\dot{r}$ , defined as the local velocity at which the propellant surface recedes, is modeled using the empirical Saint-Robert's law:

$$\dot{r} = a \cdot P_c^n \quad (3)$$

The parameters  $a$  and  $n$  are derived from empirical results for the specific propellant mixture that is used. Their values signify the sensitivity of the burn rate to pressure<sup>[6, 4]</sup>.

## 2.3 Surface Regression Depth

Given a time step increment  $\Delta t$  [s], the depth of surface regression  $dr$  during this time interval is given by:

$$dr = \dot{r} \cdot \Delta t \quad (4)$$

The cumulative burnback depth  $r(t)$  evolves over time according to this relation.

## 2.4 Thrust Evaluation

The instantaneous thrust is derived from the integral form of the axial momentum equation applied to a control volume intersecting the nozzle exit plane. Assuming quasi-steady chamber conditions and uniform ambient pressure  $P_a$  on the outer control surface, the thrust  $F$  is given by:

$$F = \lambda \dot{m} U_e + [P_e - P_a] A_e \quad (5)$$

where  $\lambda \in (0, 1]$  is the nozzle divergence correction factor. For a conical nozzle with half-angle  $\alpha_d$ :

$$\lambda = \frac{1 + \cos \alpha_d}{2} \quad (6)$$

The total mass flow rate of combustion products is directly related to the propellant regression rate:

$$\dot{m} = \rho_p A_b \dot{r} \quad (7)$$

For the tubular grain configuration used in this study, the burning surface area corresponds to the inner cylindrical area of the propellant:

$$A_b(t) = \pi D_{in}(t) L \quad (8)$$

where  $D_{in}(t)$  is the instantaneous port diameter and  $L$  is the grain length - illustrated in Fig. 1.

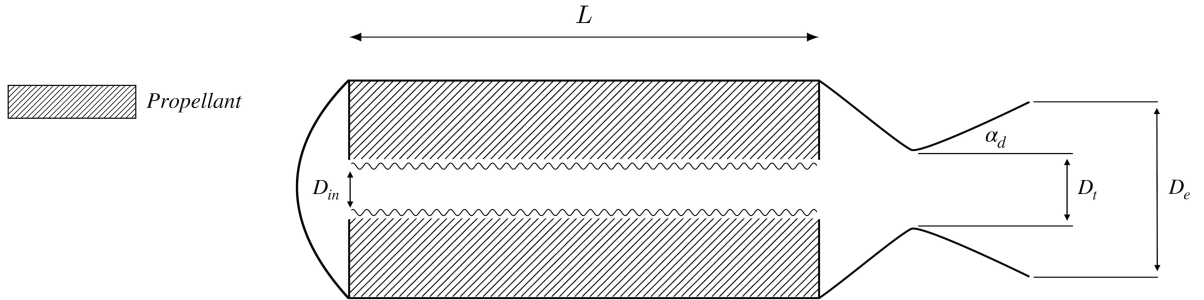


Figure 1: Geometric configuration of the tubular-grain SRM.

The thrust coefficient  $C_F$  is a dimensionless measure of nozzle efficiency, defined as:

$$C_F = \frac{F}{P_c A_t} \quad (9)$$

The coefficient reflects the ratio between the thrust produced due to gas expansion and the thrust produced by the chamber pressure acting on the throat area alone. Examining its evolution alongside the instantaneous thrust provides indication of how nozzle expansion and chamber pressure evolution affect overall motor performance.

### 3 Propellant Composition

The solid propellant investigated in this study is a composite mixture comprised of Ammonium Perchlorate (AP) serving as the oxidizer and Hydroxyl-Terminated Polybutadiene (HTPB) acting as the fuel and binder. This AP/HTPB formulation is commonly used in modern tactical and space propulsion systems due to its high energy density, mechanical resilience, and ease of processing<sup>[3, 10]</sup>. For the purposes of this work, a representative weight-based composition of 86% AP and 14% HTPB was adopted. These ratios align with typical industrial-grade composite propellants, particularly those employed in cast-grain configurations where grain geometry dictates the internal burning surface evolution<sup>[7, 8]</sup>.

To prepare the input for equilibrium chemistry simulations, each component must be represented by a simplified chemical structure that reflects its elemental composition. AP is approximated by its nominal oxidizer molecule, Ammonium Perchlorate, with the molecular formula:



HTPB, although a polymeric material with complex chain structures, is approximated by:



This approximation is widely used in equilibrium calculations and provides sufficient accuracy for global species analysis in combustion modeling.

Assuming a nominal 100 [g] batch of the propellant, the number of moles of each component can be computed using the respective molar masses: 117.49 [g mol<sup>-1</sup>] for AP and approximately 151.23 [g mol<sup>-1</sup>] for HTPB. The corresponding molar quantities are:

$$\text{mol}_{\text{AP}} = \frac{86}{117.49} \approx 0.732 \quad \text{mol}_{\text{HTPB}} = \frac{14}{151.23} \approx 0.093 \quad (12)$$

The total elemental content is obtained by multiplying the stoichiometric ratio of each molecule by its molar amount:

Element	Moles
C	$10 \times 0.093 = 0.930$
H	$15 \times 0.093 + 4 \times 0.732 = 4.323$
O	$1 \times 0.093 + 4 \times 0.732 = 3.021$
N	$1 \times 0.732 = 0.732$
Cl	$1 \times 0.732 = 0.732$

Table 2: Total elemental content (pre-normalization)

These values are then normalized by the total number of moles to yield mole fractions suitable for input into equilibrium solvers such as NASA’s CEA code:

Element	Normalized Mole Fraction
C	0.096
H	0.444
O	0.310
N	0.075
Cl	0.075

Table 3: Normalized elemental mole fractions

In addition, the oxidizer-to-fuel (O/F) mass ratio, a key design parameter in solid propulsion, is calculated based on the weight composition:

$$O/F = \frac{m_{\text{AP}}}{m_{\text{HTPB}}} = \frac{86}{14} \approx 6.14 \quad (13)$$

This value lies within the typical range for optimized AP/HTPB composite propellants<sup>[5, 11]</sup>.

## 4 CEA-Based Thermochemical Analysis

To evaluate the thermochemical behavior of the AP/HTPB composite propellant, a combustion simulation was conducted using NASA’s *Chemical Equilibrium with Applications* (CEA) code [9]. The goal was to determine key performance parameters—such as flame temperature, characteristic velocity, and product species composition—based on the elemental structure of the formulation.

The simulation was conducted in `rocket equilibrium` mode under *chamber-only* conditions, with *frozen equilibrium* assumptions and no nozzle expansion. The operating pressure was fixed at  $P_c = 7$  MPa, reflecting typical tactical-class SRM operating regimes. The input elemental composition was derived from the normalized mole fractions computed in Section 3.

The CEA output provided the following key parameters:

- **Adiabatic flame temperature:**  $T_c = 3273$  [K]
- **Characteristic velocity:**  $c^* = 1550$  [m s<sup>-1</sup>]
- **Vacuum specific impulse (estimated):**  $I_{sp} \approx 275$  [s]

These values are consistent with experimental data and previous modeling efforts for AP/HTPB systems [7, 11]. The dominant gaseous combustion products predicted at 7 MPa are listed in Table 4.

Species	Mole Fraction
H <sub>2</sub> O	0.40
HCl	0.15
CO <sub>2</sub>	0.18
CO	0.10
N <sub>2</sub>	0.12
Cl <sub>2</sub>	0.05

Table 4: Equilibrium combustion products at 7 MPa (CEA output)

The results serve as inputs for the numerical framework discussed in the following sections.

## 5 Empirical Burn Rate Parameters

The burn rate model employed in this work is based on the empirical power-law relation previously introduced in Section 2.2, where the regression velocity  $\dot{r}$  is expressed as a function of local chamber pressure. This formulation requires two constants: the pre-exponential coefficient  $a$  and the pressure exponent  $n$ . Both constants strongly depend on the physical properties of the propellant, including the size distribution of oxidizer particles, binder formulation, and particle packing density.

A wide range of  $(a, n)$  values for AP/HTPB composite propellants has been reported in the literature. Table 5 summarizes representative values derived from experimental and numerical studies covering various particle size distributions and combustion models.

Source	AP Type	$a$ [mm MPa <sup><math>n</math></sup> s <sup>-1</sup> ]	$n$
Zhang et al. (2021) <sup>[6]</sup>	Mixed AP	$5.2 \times 10^{-4}$	0.45
Dillier et al. (2019) <sup>[12]</sup>	Fine + Coarse	$7.1 \times 10^{-4}$	0.58
Morrow (2017) <sup>[8]</sup>	Coarse AP	$3.8 \times 10^{-4}$	0.38
Cao et al. (2015) <sup>[7]</sup>	Fine AP	$6.0 \times 10^{-4}$	0.50
Gross et al. (2013) <sup>[10]</sup>	Micro/meso model	$4.5 \times 10^{-4}$	0.42
Thakre & Yang (2008) <sup>[5]</sup>	Simulated	$4.1 \times 10^{-4}$	0.46

Table 5: Empirical burn rate parameters for AP/HTPB propellants

Figure 2 illustrates the sensitivity of the burn rate to chamber pressure for various  $(a, n)$  pairs across the range of 1–10 MPa. The slope of each curve reflects the pressure sensitivity: a higher exponent  $n$  yields a steeper increase  $\dot{r}$  with pressure. For example, the model by Dillier et al. (2019) shows a strong dependence on pressure, while the model by Morrow (2017) indicates weaker sensitivity, consistent with coarse AP particles that burn more steadily. The formulation proposed by Zhang et al. (2021) presents a balanced behavior suitable for mixed-particle systems.

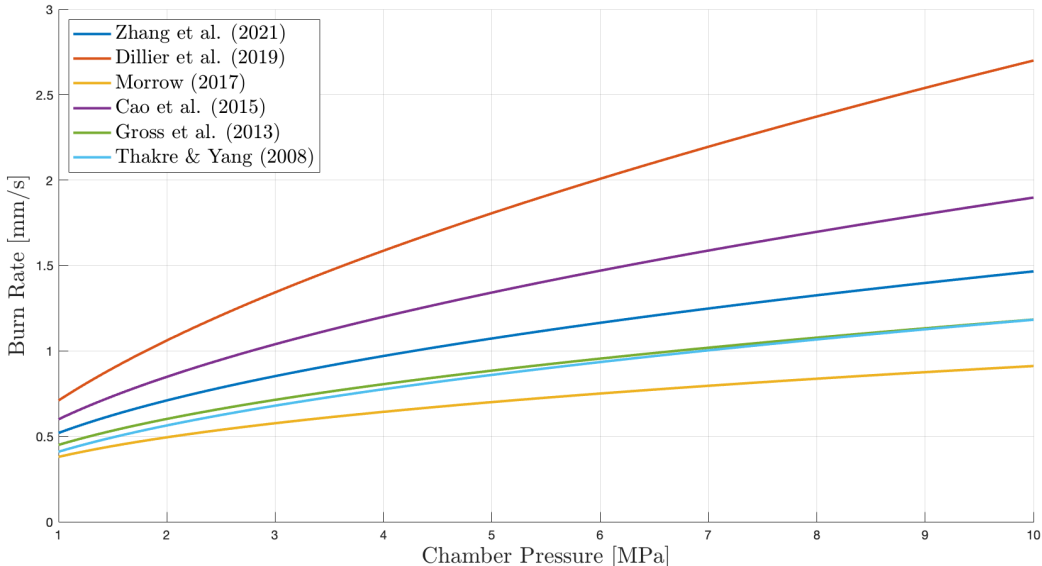


Figure 2: Burn rate vs. chamber pressure for various AP/HTPB models.

Physically, the coefficient  $a$  scales the baseline burn rate and is influenced by factors such as binder type and thermal conductivity, while the exponent  $n$  governs the rate’s sensitivity to pressure changes. Though often interrelated, each parameter reflects distinct material-level phenomena and must be carefully selected to match the targeted propellant formulation [4, 3].

For the present work, the model proposed by Zhang et al. (2021) was selected, namely:

$$a = 5.2 \times 10^{-4} \quad ; \quad n = 0.45 \quad (14)$$

This choice aligns with the assumed composition (86% AP, 14% HTPB), and offers a compromise between pressure sensitivity and combustion stability. The corresponding burn rate curve fits well within the pressure range of 3–10 MPa, which characterizes the operating envelope of many tactical-class solid motors.

## 6 Numerical Framework

The numerical simulations in this study were conducted using **Arion**, an unstructured finite-volume solver developed for compressible, reacting, multi-species flows with dynamically evolving geometries. This framework enables high-fidelity resolution of internal flowfields in SRMs, particularly where surface regression leads to substantial chamber volume evolution.

Two computational configurations were considered: an axisymmetric representation of the cylindrical grain and a three-dimensional quarter-cylinder model of the full motor. In both cases, the grain burns radially outward from the inner port surface, with the mesh dynamically updated at each time step to capture the regressing boundary. The flow, chemistry, and geometry are tightly coupled, resulting in a dynamic internal ballistic system that reflects a realistic burnback phenomenon.

### 6.1 Governing Models

The flow is governed by the compressible Reynolds-Averaged Navier–Stokes (RANS) equations, where turbulence effects are modeled statistically via ensemble-averaging. Turbulence closure is provided by the  $k$ - $\omega$  Shear Stress Transport (SST) model<sup>[13]</sup>, which offers accurate predictions in both boundary layers and separated regions, making it particularly suitable for internal reacting flows.

Convective fluxes are discretized using the AUSM-DV (Advection Upstream Splitting Method – Dissipation Vector) scheme, ensuring robust performance in compressible regimes with shocks and expansions. Inviscid Jacobians are evaluated using the Steger-Warming scheme, and second-order spatial accuracy is maintained through linear reconstruction based on Green–Gauss or diamond-cell gradient approximations. To preserve monotonicity near steep gradients, the MLP-3D limiter is employed.

Time integration is handled by an implicit, matrix-free GMRES solver using the PETSc library. Preconditioning is applied using an additive Schwarz method with ILU(2) decomposition, with solver configurations optimized separately for each subsystem, including flow, turbulence, and grid motion.

## 6.2 Thermochemical Modeling

Thermodynamic closure is achieved through Arion’s built-in tabulation framework, which enables rapid evaluation of thermodynamic states without solving chemical kinetics explicitly. Instead, precomputed property tables defined over a pressure–temperature grid are used. These tables provide essential quantities such as enthalpy, specific heat, and internal energy, thereby maintaining both numerical efficiency and thermodynamic consistency.

The property tables are initialized based on representative combustion conditions, calibrated against independent results from NASA’s CEA code<sup>[9]</sup>. This approach ensures that the simplified thermodynamic model accurately reflects the global behavior of the AP/HTPB propellant system, while avoiding the complexity associated with finite-rate chemical kinetics.

During the simulation, thermodynamic quantities are interpolated from the tables based on local pressure and temperature fields. Species transport equations are solved for the major combustion products, enabling accurate representation of spatial variations in composition and enthalpy throughout the domain.

## 6.3 Computational Grid & Boundary Conditions

### 6.3.1 2D Axisymmetric Structured Grid:

The computational mesh consists of 20 cells in the radial direction and 101 cells axially, resulting in a uniform grid with a single cell in the circumferential direction. The domain is treated as axisymmetric and simulates a longitudinal section of the cylindrical grain. Figure 3 shows the mesh layout and coordinate system.

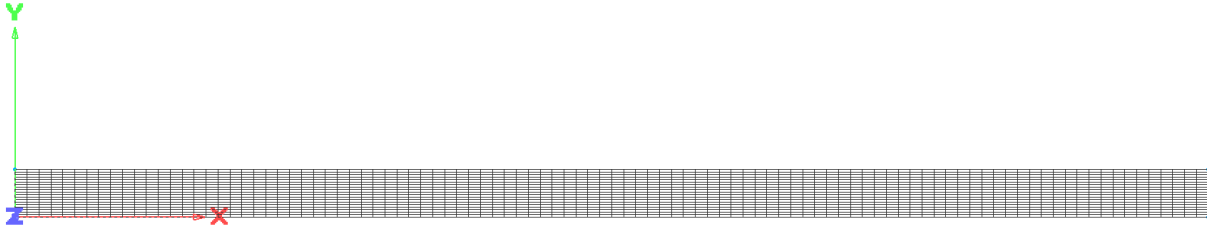


Figure 3: 2D axisymmetric computational grid: 20 (radial)  $\times$  101 (axial) cells.

The domain is bounded by five physical surfaces, each assigned a specific boundary condition reflecting its physical role within the internal flow field:

- **Burning surface:** The inner port wall, representing the regressing propellant surface, is defined as an inflow boundary. The velocity imposed here is based on precomputed tables corresponding to the local burnback rate, thereby simulating the gas-phase injection resulting from solid surface regression.
- **Inlet plane:** The upstream axial boundary is treated as a subsonic inflow. This boundary supports the initialization of internal flow structures and preserves flow continuity near the grain head. Constant stagnation conditions are prescribed to stabilize the solution at the entrance.
- **Outlet plane:** The downstream boundary is treated as a supersonic outflow, allowing characteristic-based extrapolation of flow variables without imposing back pressure. This ensures a non-reflecting condition that permits the free exit of combustion products.
- **Axis of symmetry:** Along the central radial axis of the chamber, reflective symmetry is applied to enforce the geometric and physical constraints of axisymmetric flow.
- **Transverse plane:** The circumferential thickness of the domain is modeled using a single-cell layer with planar symmetry imposed in the azimuthal direction. This effectively reduces the problem to a two-dimensional axisymmetric representation.

The initial thermodynamic state is prescribed using the reference chamber conditions obtained from CEA equilibrium analysis, with pressure and temperature set to  $P_c = 7$  MPa and  $T_c = 3273$  K, respectively. The flow field is initialized at a low subsonic velocity, corresponding to a Mach number of 0.2, which reflects the typical near-surface behavior within the combustion chamber. Turbulent quantities are initialized with standard estimates for moderate-Reynolds-number reacting flows, providing a physically consistent starting point for flow development.

### 6.3.2 3D Multi-Block Unstructured Grid

Extending the axisymmetric framework, a three-dimensional computational grid was constructed to capture the inherent three-dimensional effects of grain burnback. Only a quarter of the cylindrical motor was modeled, exploiting symmetry to reduce computational cost whilst maintaining geometric fidelity. The mesh uses a multi-block strategy, combining structured and unstructured domains depending on geometric complexity. Figure 4 shows the overall topology.

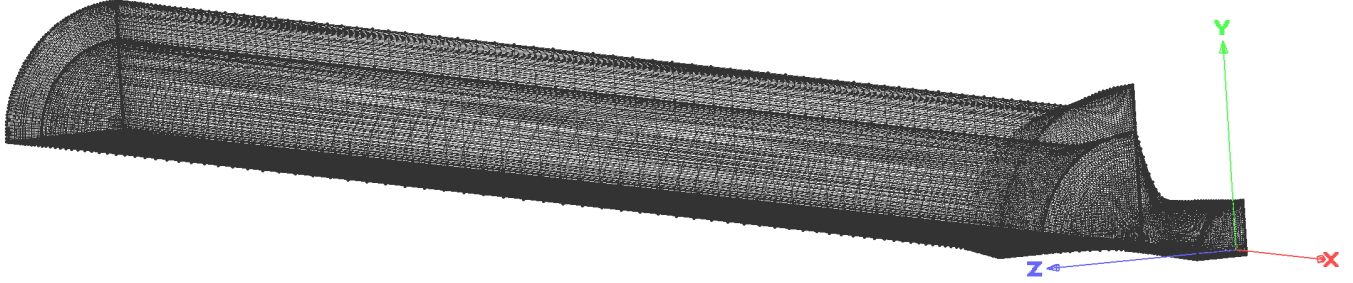


Figure 4: 3D quarter cylinder multi-block grid.

The grid is decomposed into three blocks connected through conformal interfaces to maintain solution continuity:

- **Block 1: Burning Surface Layer**

A structured quarter-cylinder block aligned with the propellant port. This block is updated at each burnback step to follow the regressing surface.

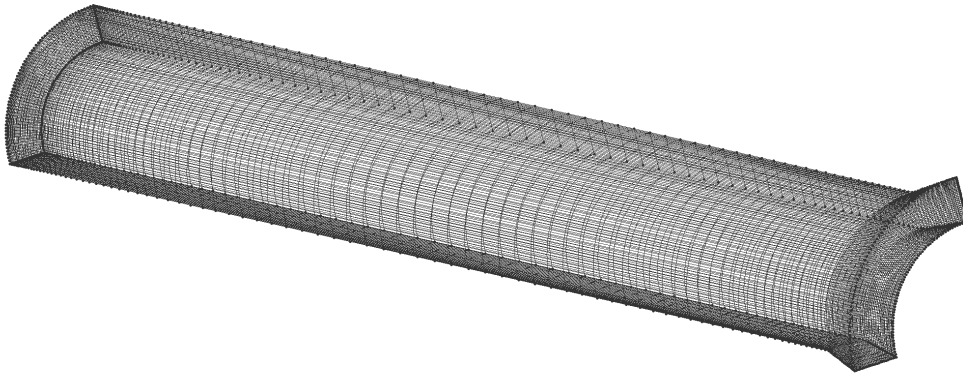


Figure 5: Block 1: 111 (axial)  $\times$  30 (radial)  $\times$  61 (circumferential) cells.

- **Block 2: Combustion Chamber**

A structured cylindrical core that spans from the head-end to the nozzle entrance. The curved sidewalls are represented by unstructured domains that remain conformal to the structured interior, providing a clean fit to the geometry and avoiding skewed cells near junctions.

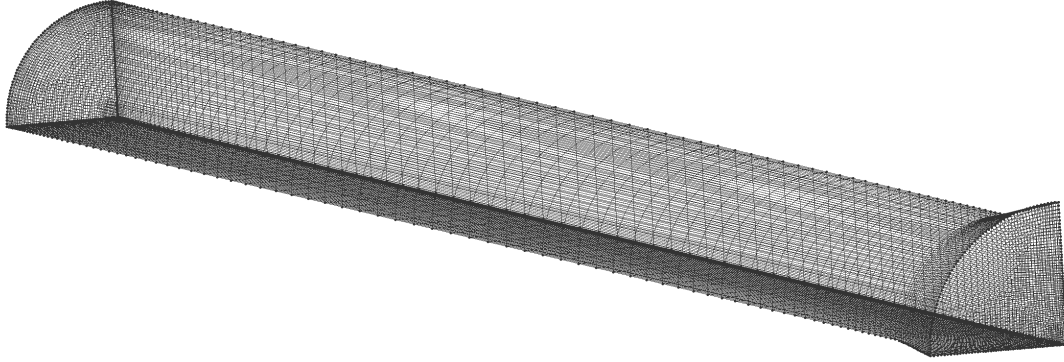


Figure 6: Block 2: 111 (axial)  $\times$  57 (radial)  $\times$  61 (circumferential) cells.

- **Block 3: Nozzle**

A convergent–throat–divergent block. The core remains structured, while the curved nozzle walls are captured with unstructured domains.

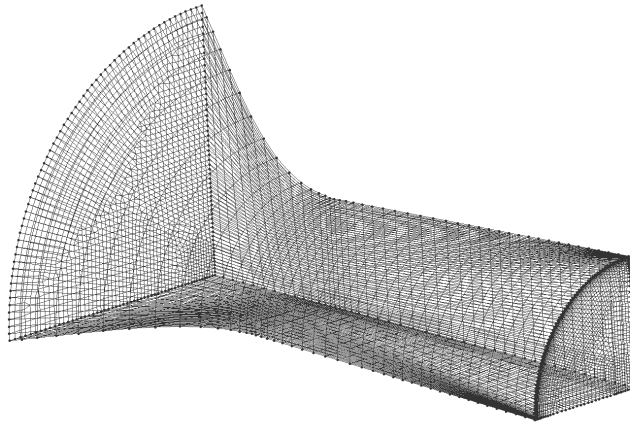


Figure 7: Block 3: 45 (axial)  $\times$  57 (radial)  $\times$  61 (circumferential) cells.

Boundary conditions follow the same rationale as in the axisymmetric case, adapted to the quarter-cylinder geometry:

- **Burning surface:** Inner port wall treated as an inflow boundary, with regression rates imposed from tabulated data.
- **Head-end plane:** Stagnation inflow condition at  $M = 0.2$ ,  $T_0 = 3273$  K, and  $p_0 = 7.0$  MPa.
- **Nozzle exit:** Supersonic outflow boundary condition.
- **Chamber and nozzle walls:** No-slip boundary condition.
- **Symmetry planes:** Reflective symmetry enforced on the two orthogonal planes bounding the quarter domain.
- **Block interfaces:** Conformal connectors applied at inter-block boundaries.

Initialization of thermodynamic and flow fields follows the same procedure as in the 2D case, using equilibrium CEA conditions for chamber pressure and temperature with a low-subsonic velocity profile. This ensures consistency between 2D and 3D cases, enabling direct comparison of burnback and pressure evolution.

## 6.4 Burnback Modeling and External Coupling Framework

The evolution of the burning surface is captured through a mesh motion module embedded in the solver framework. At each time step, the chamber pressure is sampled and used to evaluate the local regression velocity based on the empirical burn rate model defined in Section 2.2. The resulting displacement is then computed according to Equation (2).

The entire process is coordinated externally through a Python script, which automates the extraction of pressure data, computation of regression velocity, and the feeding of a new boundary displacement into the solver.

The external coupling proceeds according to the following stages:

1. **Initialization:** The simulation begins by defining the initial geometry, thermodynamic state, and gas properties, based on tabulated combustion data extracted from equilibrium analysis. Input files and mesh configurations are generated accordingly.
2. **Flow Solution:** The solver runs a fixed number of numerical iterations while keeping the mesh static. These iterations are sufficient to achieve quasi-steady convergence for the current burn geometry. The total physical time advanced in each cycle is computed as:

$$\Delta t_{\text{physical}} = \Delta t_{\text{numerical}} \times N_{\text{iterations}}$$

3. **Field Extraction:** Once the cycle completes, the pressure distribution along the regressing surface is extracted and stored.
4. **Surface Regression Evaluation:** Local regression velocities are calculated from the sampled pressure values, and the resulting displacements are obtained over the physical time interval.
5. **Mesh and Inflow Update:** The mesh is deformed accordingly, and updated boundary conditions—including pressure tables—are regenerated for the next run.
6. **Cycle Advancement:** The simulation proceeds to the next loop step using the updated geometry and inflow profile. This sequence continues until the desired maximal regression depths is simulated.

A schematic representation of this process provided in the Appendix, illustrating the full external coupling strategy.

## 6.5 Cross-Validation using HyPE

To validate the accuracy of Arion’s external burnback model, results were compared against those obtained from **HyPE**, a well validated structured solver designed for reactive and thermochemically complex flows. Unlike Arion, HyPE features native support for surface regression through its `surface.reaction` module, which directly computes surface displacement based on local pressure fields.

To ensure a consistent comparison, both solvers were configured with identical thermodynamic properties, mixture compositions, and burn rate parameters.

## 7 Results

This section presents numerical results obtained with the externally coupled Arion solver for both 2D (axisymmetric) and 3D (quarter-cylinder) configurations. The analysis addresses the evolution of propellant regression, validation of Arion against the reference HyPE solver, and the effect of extending the formulation to three dimensions. In addition, motor performance is assessed using 3D-derived histories of instantaneous thrust and thrust coefficient. Together, these results provide a comprehensive validation of the solver's predictive capability and the physical consistency of the simulated SRM flowfield.

### 7.1 Global Propellant Recession

Figure 8 shows the maximum propellant recession as a function of time for Arion (2D, 3D) and HyPE. All three predict a smooth, nearly linear progression, consistent with the quasi-steady nature of SRM operation<sup>[7, 8]</sup>. The curves nearly overlap with negligible differences in magnitude.

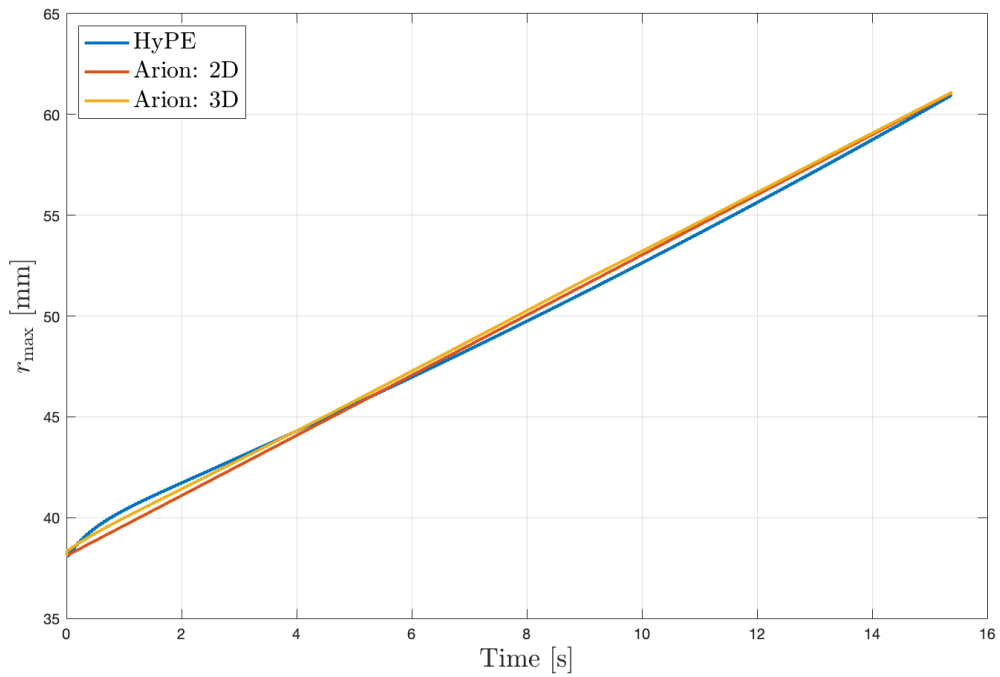
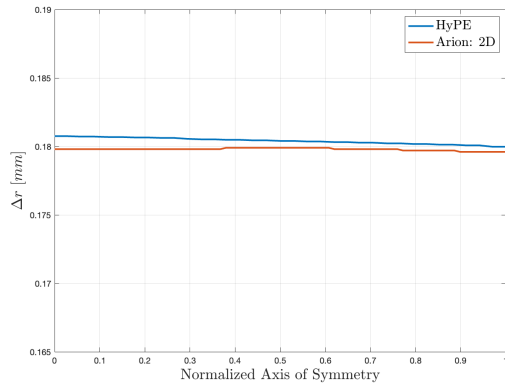


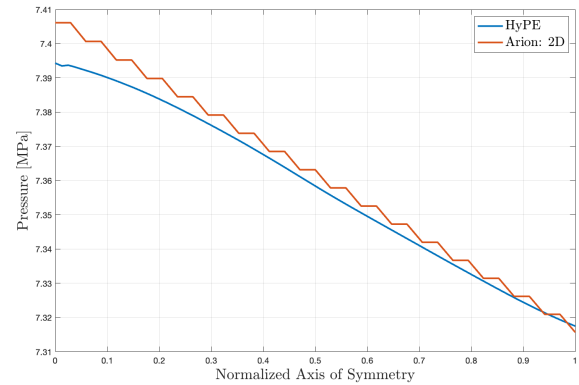
Figure 8: Maximum propellant recession  $r_{\max}(t)$  predicted by Arion (2D, 3D) and HyPE.

## 7.2 Validation against HyPE

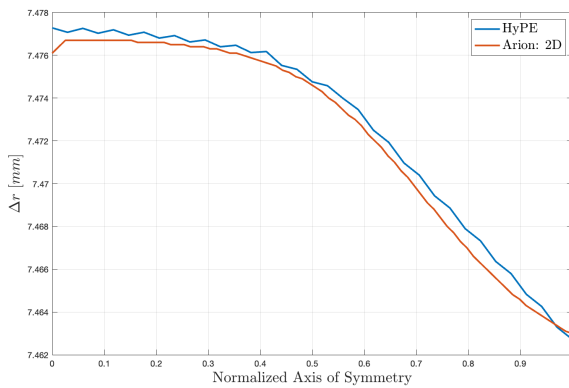
Figure 9 compares the axial burnback depth  $\Delta r(x)$  and the pressure distribution  $P(x)$  for Arion (2D) and HyPE at three representative times:  $t = 0.06$ , 4.99, and 15.39 seconds.



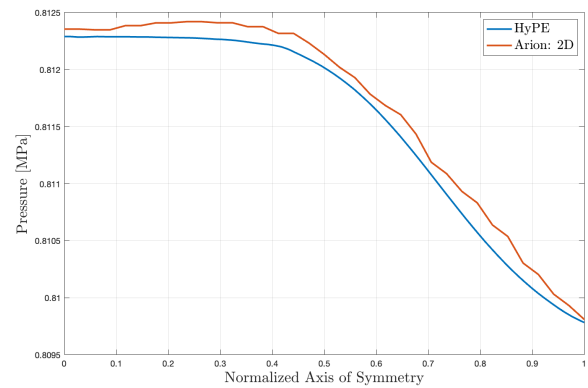
(a) Burnback depth at  $t = 0.06$  s



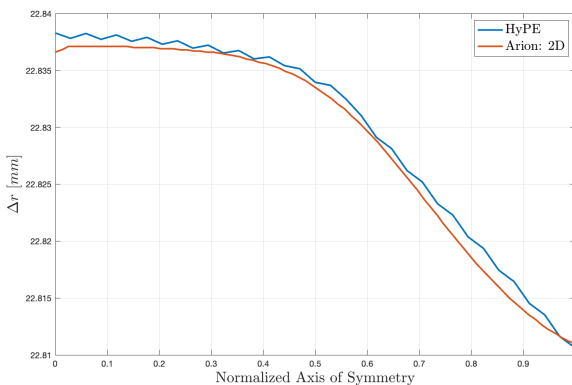
(b) Pressure at  $t = 0.06$  s



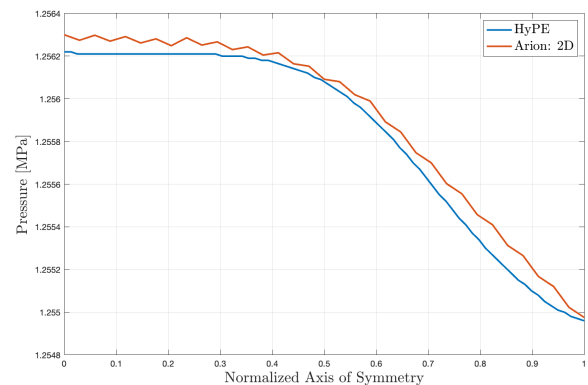
(c) Burnback depth at  $t = 4.99$  s



(d) Pressure at  $t = 4.99$  s



(e) Burnback depth at  $t = 15.39$  s



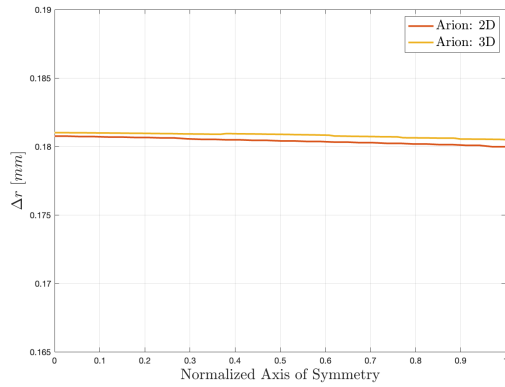
(f) Pressure at  $t = 15.39$  s

Figure 9: Comparison of axial regression and pressure distributions at selected times: Arion (2D) vs. HyPE.

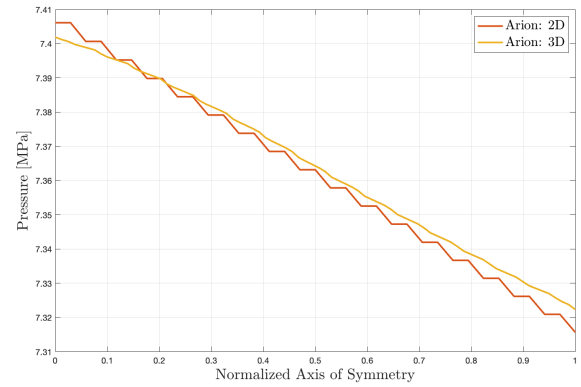
The results indicate an overall strong agreement between the two solvers. Firstly, both solvers demonstrate similar pressure variations, characterized by peak values near the chamber inlet, as well as a gradual decrease toward the nozzle. Moreover, even though minor deviations in burnback distributions between HyPE and Arion become more noticeable over time, the general burnback trends remain consistent.

### 7.3 Effect of 3D Extension

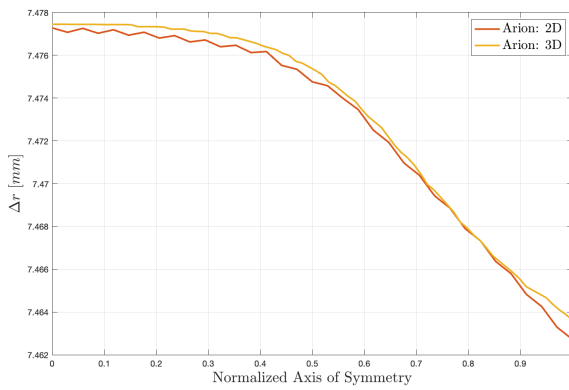
To assess the effect of extending the solver to three dimensions, results from the 3D quarter-cylinder configuration were compared against the corresponding 2D Arion solution. Figure 10 presents this comparison:



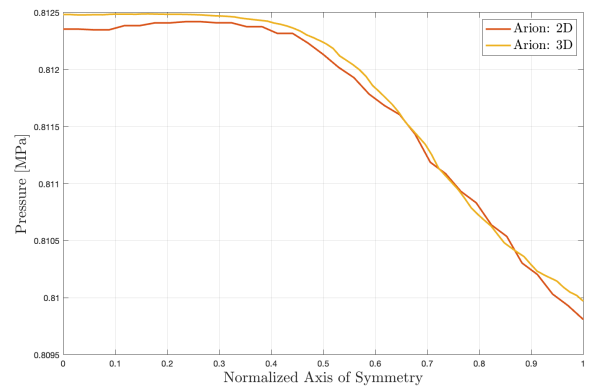
(a) Burnback depth at  $t = 0.06$  s



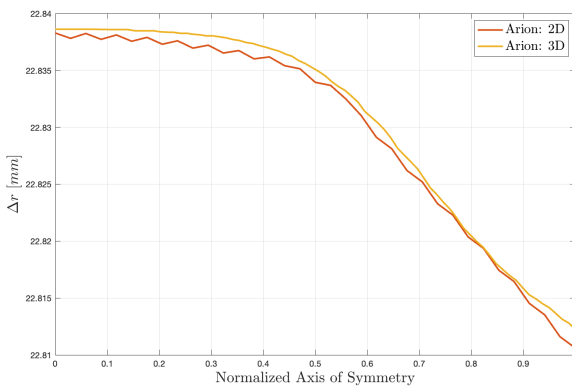
(b) Pressure at  $t = 0.06$  s



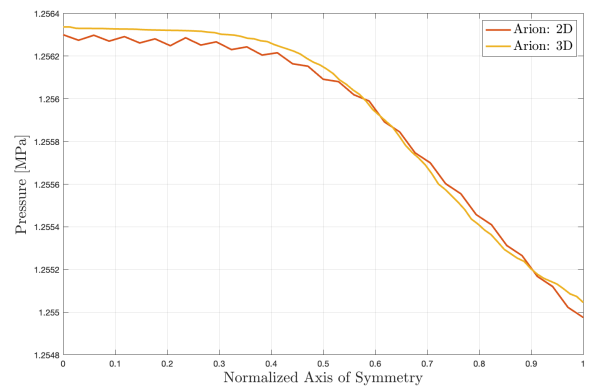
(c) Burnback depth at  $t = 4.99$  s



(d) Pressure at  $t = 4.99$  s



(e) Burnback depth at  $t = 15.39$  s



(f) Pressure at  $t = 15.39$  s

Figure 10: Comparison of axial regression and pressure distributions at selected times: Arion (2D vs. 3D).

Across all times, the 3D results closely align with the 2D predictions, confirming that the underlying axisymmetric physical properties are preserved. The only noticeable difference is that the 3D fields appear slightly smoother, reflecting the additional circumferential resolution of the 3D grid, which suppresses small numerical oscillations without changing the physical trends.

## 7.4 Thrust Profile

The thrust and thrust coefficient were evaluated based on data from the 3D quarter-cylinder configuration. To obtain the total thrust of the full motor, the integrated forces over the nozzle exit of the simulated quarter-domain were multiplied by four, exploiting the geometric symmetry of the configuration.

Parameter	Value
Throat diameter	0.026 [m]
Exit diameter	0.040 [m]
Grain length	0.680 [m]
Nozzle divergence half-angle	5°
Ambient pressure	101,325 [Pa]

Table 6: Geometric and boundary parameters of the simulated SRM.

The instantaneous chamber pressure  $P_c(t)$  was extracted directly from the simulation, along with the exit static pressure  $P_e(t)$ , exit velocity  $U_e(t)$ , and propellant density  $\rho_p(t)$ . These quantities were post-processed according to the formulation presented in Section 2.4 to compute the total thrust and corresponding thrust coefficient.

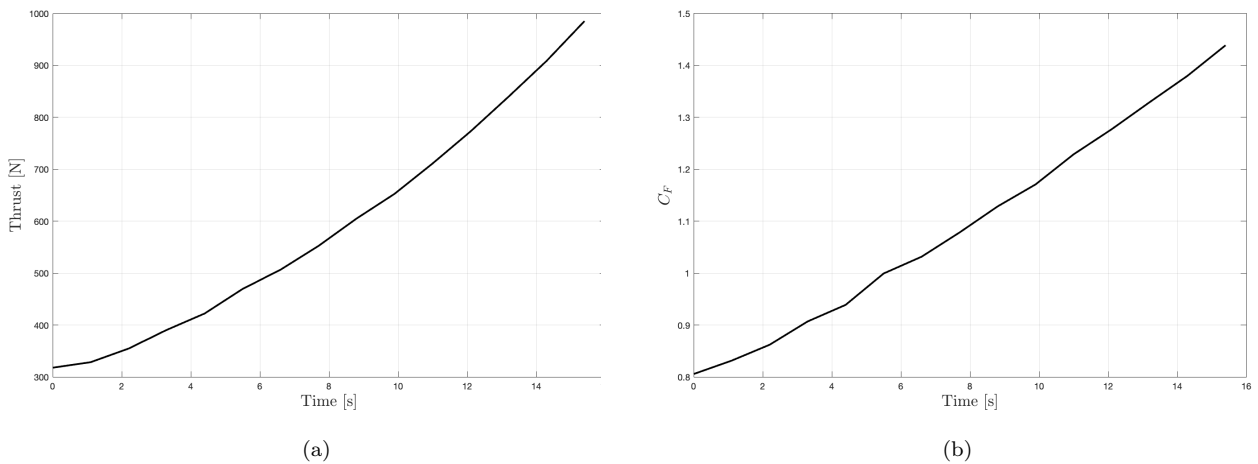


Figure 11: (a) Instantaneous thrust  $F(t)$  and (b) thrust coefficient  $C_F(t)$  obtained from the 3D quarter-cylinder simulation and scaled to full motor.

The thrust curve exhibits a monotonic increase throughout the burn as the burning surface area expands, causing the chamber pressure and mass flow rate to rise. At early times, a slightly lower  $C_F$  is observed, likely due to partial flow separation near the nozzle lip under over-expanded conditions. As the chamber pressure builds, the flow fully attaches and  $C_F$  rises steadily, indicating enhanced expansion efficiency as the chamber-to-ambient pressure ratio evolves. These results are consistent with the regression and pressure fields discussed above.

## 7.5 Physical Validation

Both simulations were executed in cycles of 100 numerical steps, each with a calibrated time step of  $\Delta t_{\text{numerical}} = 0.0015$  s, corresponding to a physical step size of  $\Delta t_{\text{physical}} = 0.15$  s per cycle. The total burn time reached approximately 15.4 s, with a final propellant recession of about 60 mm.

These values are consistent with reported burn durations and propellant utilization for tactical-class AP/HTPB solid motors operating at 6–8 MPa<sup>[4, 7, 6]</sup>. Previous experiments and simulations indicate recession depths of 40–70 mm over comparable time frames, supporting the physical credibility of the present results.

The thrust evolution exhibits the progressive profile characteristic of tubular-grain motors, consistent with experimentally reported behaviour in the literature<sup>[14]</sup>. The computed  $C_F$  values align with reported trends for comparable nozzle expansion ratios and chamber pressures<sup>[1]</sup>, providing further confidence in the physical fidelity of the solution.

## 8 Conclusions

This work presented a numerical framework for simulating internal ballistics in solid rocket motors with dynamically evolving geometries. The Arion solver was extended through a Python-based script that integrates empirical burnback models, pressure feedback, and mesh deformation, while maintaining thermodynamic consistency using pre-tabulated combustion data.

Validation against HyPE demonstrated excellent agreement across key metrics, including pressure profiles and regression depth evolution, confirming the accuracy and stability of the developed approach. Extending the framework from 2D to a full 3D quarter-cylinder grid served as a critical consistency check: the 3D results reproduced the 2D and HyPE predictions with nearly identical global recession histories and matching pressure and burnback distributions. The 3D fields appeared slightly smoother, a consequence of the higher effective resolution, but the underlying physics remained unchanged. This demonstrates that the solver maintains its predictive capability in three dimensions, which is essential for future applications involving complex non-axisymmetric grain designs where a 2D approximation is no longer sufficient.

The obtained thrust and thrust coefficient reinforce the physical validity of the framework. The computed thrust exhibits the progressive behaviour characteristic of tubular-grain motors, while the corresponding  $C_F$  values remain consistent with physically realistic performance for comparable expansion ratios and chamber pressures. These results confirm that the extended framework accurately captures both the detailed flowfield evolution and the integral ballistic response of the motor.

Overall, the findings demonstrate that an externally managed regression framework, when properly calibrated and validated, can replicate the accuracy and stability of traditional in-solver implementations. The developed framework is robust, modular, and well suited for extension to more complex grain configurations, multi-physics coupling, and advanced internal ballistics research.

## References

- [1] G. Sutton and O. Biblarz, *Rocket Propulsion Elements*. Wiley, 9th ed., 2016.
- [2] D. Deb, B. Singh, and A. Bhaduri, “Computational prediction of internal ballistics in solid rocket motors using a coupled pressure–regression rate model,” *Aerospace Science and Technology*, vol. 125, p. 107294, 2022.
- [3] L. Zhang, J. Wang, and X. Li, “Review on combustion mechanisms and models of composite solid propellants,” *Progress in Energy and Combustion Science*, vol. 80, p. 100879, 2020.
- [4] T. Wilson and M. Beckstead, “Modeling the burning rate of composite solid propellants,” *Combustion and Flame*, vol. 156, no. 2, pp. 417–427, 2009.
- [5] W. Cai, P. Thakre, and V. Yang, “A model of ap/htpb composite propellant combustion in rocket-motor environments,” *Combustion Science and Technology*, vol. 180, no. 11, pp. 2002–2025, 2008.
- [6] J. Yuan, J. Liu, Y. Zhou, Y. Zhang, and K. Cen, “Thermal decomposition and combustion characteristics of al/ap/htpb propellant,” *Journal of Thermal Analysis and Calorimetry*, vol. 143, no. 4, pp. 1623–1633, 2021.
- [7] Y. Cao, Y. Yu, and R. Ye, “Numerical analysis of ap/htpb composite propellant combustion under rapid depressurization,” *Applied Thermal Engineering*, vol. 78, pp. 209–217, 2015.
- [8] G. Morrow, *Correlating the Effects of AP Particle Size and Concentration on AP/HTPB Composite Propellant Burning Rates*. PhD thesis, Texas A&M University, 2017.
- [9] S. Gordon and B. J. McBride, “Computer program for calculation of complex chemical equilibrium compositions and applications i. analysis,” Tech. Rep. NASA-RP-1311, NASA Lewis Research Center, 1994. NASA Reference Publication 1311.
- [10] M. Gross, T. Hedman, S. Son, T. Jackson, and C. Masser, “Coupling micro and meso-scale combustion models of ap/htpb propellants,” *Combustion and Flame*, vol. 160, no. 7, pp. 1405–1415, 2013.
- [11] C. Vijay and P. Ramakrishna, “Estimation of burning characteristics of ap/htpb composite solid propellant using a sandwich model,” *Combustion and Flame*, vol. 214, pp. 293–304, 2020.
- [12] C. Dillier, E. Petersen, T. Sammet, and J. Thomas, “Very-high-pressure burning rates of ap/htpb-composite propellants with varying ap particle sizes and distributions,” in *AIAA Propulsion and Energy Forum*, American Institute of Aeronautics and Astronautics, 2019.
- [13] F. R. Menter, “Two-equation eddy-viscosity turbulence models for engineering applications,” *AIAA Journal*, vol. 32, no. 8, pp. 1598–1605, 1994.
- [14] P. G. Hill and C. R. Peterson, *Mechanics and Thermodynamics of Propulsion*. Addison-Wesley Publishing Company, 2 ed., 1970.

# Appendix

## Python Code Flowchart

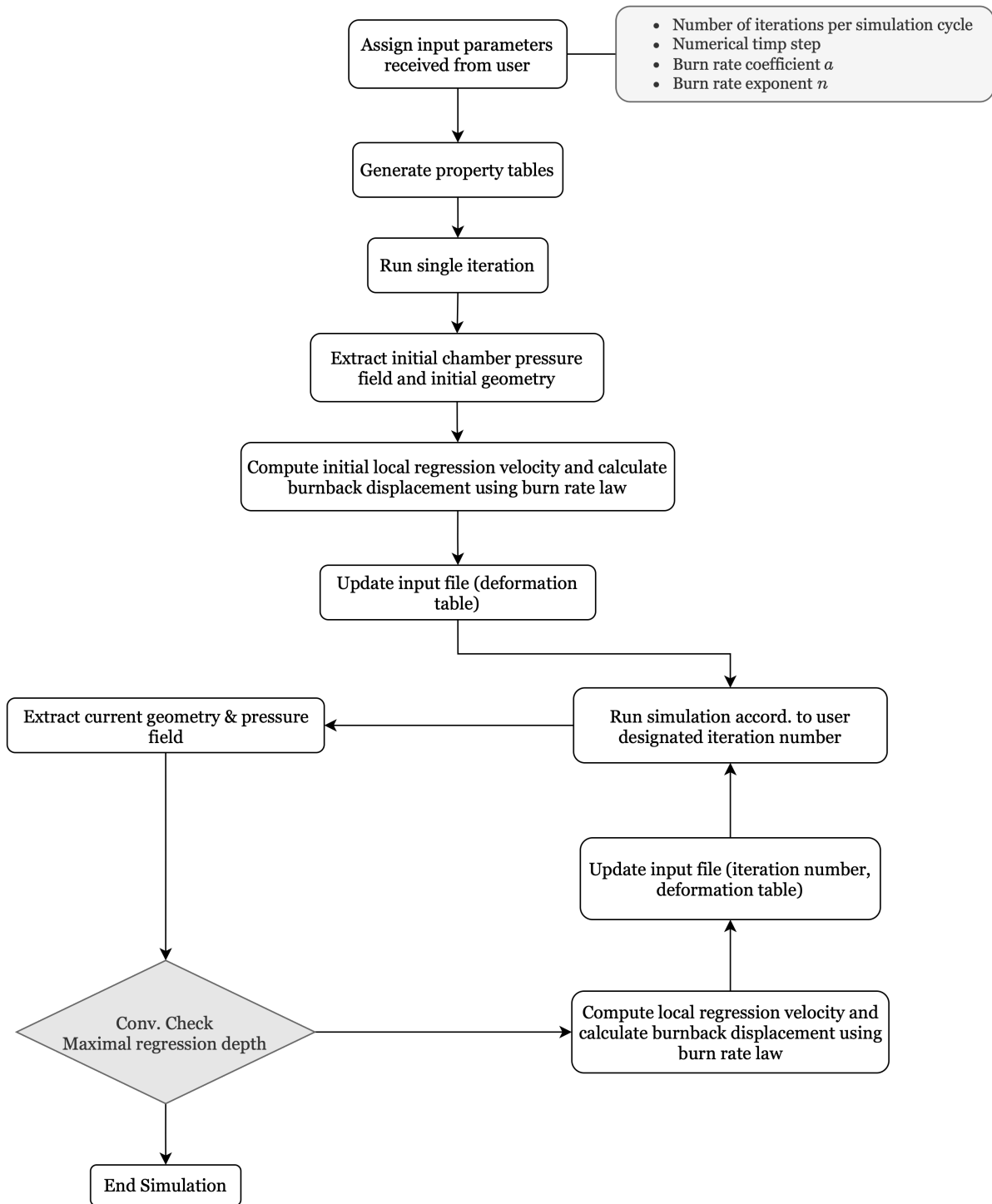


Figure 12: Schematic representation of Arion's externally-coupled burnback model.